

# Voigt profile characterization of copper $K\alpha$

A J Illig, C T Chantler and A T Payne

School of Physics, The University of Melbourne, Melbourne, Australia

E-mail: [aillig@unimelb.edu.au](mailto:aillig@unimelb.edu.au) and [chantler@unimelb.edu.au](mailto:chantler@unimelb.edu.au)

Received 6 August 2013, in final form 12 September 2013

Published 7 November 2013

Online at [stacks.iop.org/JPhysB/46/235001](http://stacks.iop.org/JPhysB/46/235001)

## Abstract

We report a characterization of the Cu  $K\alpha$  profile and a transferable determination of the 2p satellite line using a new Voigt methodology which generates improved fits, smaller residuals and details of Compton profile features. The  $K\alpha_{1,2}$  emission of Cu was obtained from a rotating anode through a monolithic Si channel-cut monochromator. Least-squares fitting of a minimum set of Voigt profiles reached a noise limit. Sufficient statistical information and resolution permits the determination of major and minor peak components in a fully-free least-squares analysis rather than the previous constrained single peak-by-peak method. Relative energies of the component Voigts within each profile, linewidths and  $K\alpha_1/K\alpha_2$  peak intensity ratios, are compared to the previous best empirical sum of Lorentzian-slit peaks, clearly demonstrating that a sum of Voigt profiles provides a superior fit to the observed profile. 104 profiles at accelerating voltages from 20 kV through 50 kV provided a stable unique profile across the broad range of 2.5–6.25 times the characteristic energy. This robustness proves the stability of Cu  $K\alpha$  for use in high accuracy calibration, and supports the validity of the impulse approximation across this range of energy. The lineshape, contributions to noise broadening, the quantum yield and the Fano factor, relevant to spectral profiling, are discussed.

(Some figures may appear in colour only in the online journal)

## 1. Introduction

The spectral profiles obtained from characteristic radiation have long provided a window into atomic structure [1, 2] and continue to refine our understanding of quantum electrodynamics [3–5], the most thoroughly tested theory in nature. The  $K\alpha$  transitions serve as standard calibration sources for high accuracy laboratory physics, x-ray spectroscopy, and as astrophysical markers. The absolute energies of the profile peaks, as well as their energy differences, are used as calibration standards in wavelength-dispersive x-ray experiments [6, 7]. Intriguingly, the dominant transitions exhibit strong asymmetries in their intensity profiles, especially in the 3d transition metals, which continue to challenge advanced atomic and condensed matter physics theory.

$K\alpha$ , the  $2p \rightarrow 1s$  transition, has fine structure splitting in the 2p subshell, giving  $2p_{3/2} \rightarrow 1s$  for  $K\alpha_1$  and  $2p_{1/2} \rightarrow 1s$  for  $K\alpha_2$ , with an energy separation depending on the magnitude of relativistic effects (figure 1). Statistical degeneracies predict that the integrated intensity ratio  $K\alpha_2 : K\alpha_1$  should be 0.5:1, but experimental results show an increase in this ratio with atomic number,  $Z$  [9–12]. This  $Z$ -dependence is supported by non-relativistic Hartree–Fock calculations [13, 14] when shell coupling and exchange degeneracy are taken into account. Relativistic Dirac–Hartree–Fock calculations have shown that exchange effects are also necessary to explain observed intensity ratios [15]. In addition, the  $Z$ -dependence is also manifest in the de-excitation rate of the 1s hole by capture of a  $2p_{1/2}$  electron being greater than that for capture of a  $2p_{3/2}$  electron [16]. The faster decay rate results in the linewidth of  $K\alpha_2$  being greater than that of  $K\alpha_1$  [17, 18].

Precision measurements reveal the  $K$  line profiles not to be a sharp doublet but to include innate asymmetries, in Cu [19–21] and all 3d transition metals [14, 22–26]. The asymmetry has been attributed to the creation of an additional electron hole, usually in the bombardment event, prior to

 Content from this work may be used under the terms of the [Creative Commons Attribution 3.0 licence](http://creativecommons.org/licenses/by/3.0/). Any further distribution of this work must maintain attribution to the author(s) and the title of the work, journal citation and DOI.

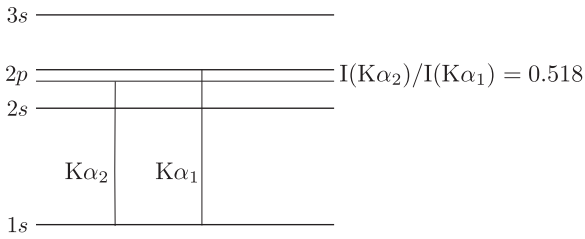


**Figure 1.**  $K\alpha$  characteristic electronic transitions for copper. Statistical predictions give 0.5:1 for  $K\alpha_2/K\alpha_1$ , however, experimental ratios of 0.518:1 [8] require significant additional physics from advanced relativistic theory for their interpretation.

decay [6, 27]. Alternate explanations involve atomic or solid state processes such as Kondo interaction of conduction band electrons with core-hole states [28], interaction in the final state between core holes and unfilled 3d shells [14], electrostatic exchange between 2p and 3d shells [29], 3l electron shake processes [30], and contributions from multi-electron satellite and hypersatellite lines [31]. Electron shake occurs when the ionized core electron is accompanied by additional excited or ionized electrons. Shake processes have been particularly supported by providing good fits to experimental data [18, 21, 30]. These correlated ionizations are major contributors to satellite lines in x-ray photoemission spectra [32–34].

Despite the need for accurate determination of shake probabilities, self-consistent field calculations show poor agreement with experimental results, especially in complex atoms [21]. Lowe and Chantler [21] have provided the first *ab initio* calculations of shake probabilities for 3d transition metals that are in good agreement with experimental results. Copper, however, remains a discrepancy. The atomic structure of copper is unusually difficult since the 3d and 4s subshell energies overlap or swap depending on the core configuration. Comparison with relativistic atomic theory is required to understand satellite asymmetries in open-shell elements [35] since relativistic effects are more pronounced as  $Z$  increases [20]. Electron correlation and exchange is manifest in the growth of coupling with increasing  $Z$ , and discrepancies between experiment and theory lead to introduction of energy offsets and dispersion scales into the spectra [19, 20, 36]. Combining precision lineshape measurements and *ab initio* relativistic Dirac–Fock calculations, Deutsch *et al* demonstrated that Cu  $K\alpha$  and  $K\beta$  emission lines can be accounted for by contributions from 3d spectator and diagram transitions [37, 38]. Chantler *et al* [16] used a relativistic Multi-Configuration Dirac–Hartree–Fock approach to address the same issue. The widespread use of Cu as a calibration and laboratory light source [31] demands that the spectrum be well understood, which requires new, more precise experimental measurements to confirm and advance theory.

Peak broadening is determined by instrumental functions, natural broadening and diffractive processes. Calibration of experimental data requires not just alignment with the maxima of the characteristic peak energies, but also accounting for systematics such as nonlinear scaling and broadening processes [8, 39]. Generally, observed spectra are fitted to a sum of line profiles whose energies and intensities are

determined by fitting rather than *ab initio*. The choice of line profile shape should reflect the broadening processes to yield a robust determination of electronic properties. We have measured to high precision the profile dependence on the excitation energy across the broad range of 2.5–6.25 times the characteristic energy, or from 20 keV through 50 keV. The profile is stable and unique—a significant observation supporting the sudden approximation across this energy range.

## 2. Experiment

Cu data was collected using x-ray radiation from a rotating Cu anode and directed through a monolithic Si channel-cut crystal (figure 2). A MacScience rotating anode passed a tube current of 10 mA through a  $0.1 \times 1 \text{ mm}^2$  tungsten filament which produced a stream of electrons targeted on a Cu anode. X-rays passed through a slit and a double-bounce Si (111) monochromator onto a Photometrics  $512 \times 512$  pixel Si CCD detector cooled with liquid nitrogen to  $-97.7^\circ\text{C}$ .

Using the lattice spacing  $d$  of Si(111) given by  $2d = 6.2712 \text{ \AA}$  [40], Bragg angles are  $14.219^\circ$  for the Cu  $K\alpha_1$  energy of 8047.78 eV and  $14.258^\circ$  for the  $K\alpha_2$  energy of 8027.83 eV. The crystal was rotated from the zero angle into the region of the predicted Bragg angles until the expected twin  $K\alpha_{1,2}$  bright lines appeared on the CCD. Once the peak lines were located, the slit was opened up and the full emission image was centred on the CCD.

Profiles were collected with exposures times of 200, 500, 1000, and 2000 ms for accelerating voltages over the 20–50 kV range in 1 kV steps for a total of 104 images. Seven background exposures were also taken, with the rotating anode off and the shutter closed, for exposure times of 10, 50, 100, 200, 500, 1000 and 2000 ms. These backgrounds were weighted by exposure time and subtracted from each profile. Background-subtracted images were cropped to isolate the  $K\alpha$  profile. The dominant lines showed a slight angle from the vertical due to rotation of the CCD plane. Pre-analysis vertically aligned the dominant lines by rotating the image in steps of  $0.005^\circ$  via a Levenberg–Marquardt least-squares fitting process of a two-peak function fit to the vertically summed profile. All images were found to have a rotation angle of  $-0.76^\circ \pm 0.01^\circ$ , minimizing the fwhm of the  $K\alpha_2$  peak.

For CCD detectors, an estimate of the quantum noise—the intrinsic variance from the number of generated photons absorbed in the detector [41, 42]—is crucial for the interpretation of noise variance, a principal contributor to peak broadening, and the  $\chi_r^2$  significance. If  $w$  is the effective energy needed to produce an electron-hole pair in the detector, also known as the quantum yield, and  $E$  is the peak energy, then the estimate of the number of hole pairs,  $\langle n \rangle$ , and its intrinsic variance are

$$\langle n \rangle = \frac{E}{w}. \quad (1)$$

Then an estimate of the correctly scaled intensity is given by

$$N_{\text{x-ray counts}} \approx N_{\text{raw counts}} / \langle n \rangle. \quad (2)$$

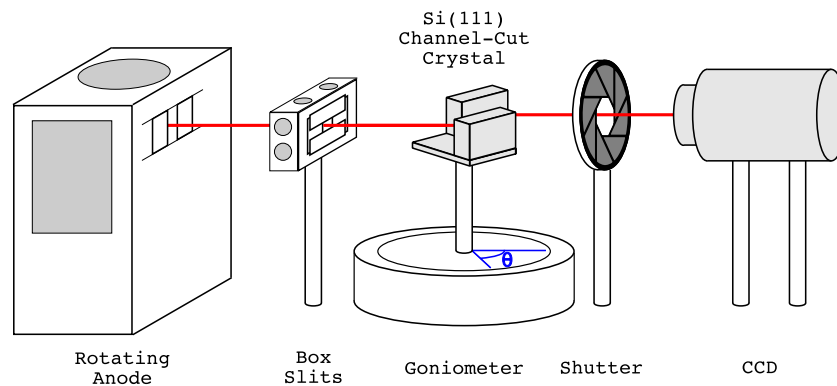


**Figure 2.** Experimental layout showing the major elements of the radiation emission and image collection process.

Values for  $w$  in Si vary significantly in the literature [43–47]. However, several sources found the quantum yield to converge to 3.8 eV near liquid nitrogen temperatures [48, 49]. Hence the profiles were scaled using  $E_{K\alpha_1} = 8047.8227(26)$  eV and  $w = 3.78(2)$  eV. We cite the quantum yield at low temperature (77 K) as it appears to be the most relevant literature claim. An estimate has suggested  $w \simeq 3.68$  eV around 175 K (our measurement temperature) which is consistent with our choice and the variability of literature.

### 3. Profile

Transition metals have asymmetric profiles with an extended tail on the low-energy side of the transmission peaks [50, 51]. Choice of profile must consider this asymmetry and both inhomogeneous and homogeneous sources of broadening. Thermal or Doppler broadening in space or energy, and the finite energy resolution of the spectrometer, are normally distributed and best represented by a Gaussian distribution. Homogeneous sources of broadening, such as lifetime, pressure or instrumental factors are often modelled by a Lorentzian lineshape. These can be convolved with aperture functions (slits) and other complex instrumental functions. While many lineshapes, such as Bragg-diffractive and the theoretical Doniac-Sunjic, display asymmetry and share features with the Gaussian and Lorentzian distributions, their respective suitability is limited by simplistic lineshape [52–54] or non-integrability [28, 55]. The best experimental description of Cu  $K\alpha$  in the literature reports profiles constructed of Lorentzians convolved with a slit function [9].

The Voigt profile, the convolution of a Gaussian and Lorentzian, represents both natural homogeneous broadening and normally distributed instrumental or source broadening. ‘Pseudo-Voigt’ profiles, such as Pearson 7 profiles, mimic the profile shapes of Voigts and are computationally simple, however the profile range is restricted and the physical basis is poor. With the computational processing power now available, there is very little justification for the continued use of such approximations and therefore the full Voigt prescription was employed in this work. A common Gaussian width has been used in the fits for all Voigt profiles and only the Lorentzian width differs from peak to peak.

Voigt profiles model the peaks quite closely. Charge collection losses can lead to a reduction in energy of observed photons [56], contributing to background with a tail on the low-energy side of transition, which could contribute to the residual and  $\chi_r^2$  (figure 3). The current data indicate dominance of Compton processes being responsible for the asymmetric shelf, which increases very slightly on the low-energy side as it approaches the  $K\alpha_2$  peak, ending in a slight peak as it reaches the tail of the  $K\alpha_2$  peak. In the high-energy tail of  $K\alpha_1$ , there is a small and distinct 2p-satellite. In 2006, Diamant *et al* [57] performed a relativistic multi-configuration Dirac–Fock modelling of the Cu satellite transitions, compared the theoretical model to experimental data and reported agreement between theory and observation for Cu  $K\alpha_{1,2}$ . The position of the 2p-satellite in figure 3 agrees with their findings. On the high-energy side of the images (beyond the plotted region), there is a sharp intensity drop in the tail of the  $K\alpha_1$  peak due to vignetting in the experimental geometry.

Incomplete charge conversion and Compton distributions are often both modelled by a complementary error function [56, 58], given by  $\text{erfc}(x) = \frac{2}{\sqrt{\pi}} \int_x^\infty e^{-t^2} dt$ . A variety of alternate fitting functions were investigated, and the complementary error function with a Compton peak best modelled the observed Compton shelf. The complementary error function is modelled by  $y = (a \times \text{erfc}(b \times (x - c)))$  where  $a = 0.63(0.28)$ ,  $b = 1.8(1.3)$ ,  $c = 27.5(3.2)$ .  $b$  and  $c$ , the horizontal stretch and shift, are given in channels. For all profiles,  $c$  was constrained to be more than  $5\sigma$  from the  $K\alpha_2$  centroid. Sequential fits of additional Voigts located one of the Voigt peaks at the Compton peak, indicating the significance and the physicality of this feature, at approximately 2.5 fwhm from the  $K\alpha_2$  peak position.

#### 3.1. Residual analysis

A Levenberg–Marquardt least-squares process [59] fitted 3–6 Voigt peaks, in addition to the complementary error function, successively until the  $\chi_r^2$  was minimized. Care was taken to determine the proper placement of the additional Voigt peaks without resorting to fixing parameters which would prevent finding a global minimum for the fit. Ergo, the residual of each total profile was analysed for the largest area of structure and position of greatest discrepancy between data and fit, providing initial estimates for each additional Voigt peak. A

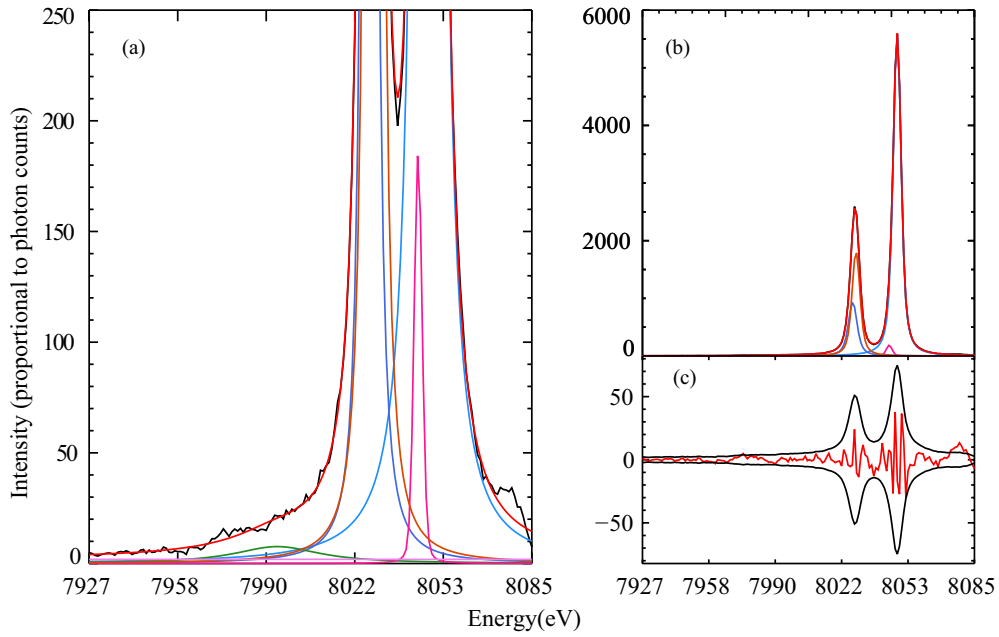


**Figure 3.** Typical fit of the 44 kV, 1000 ms exposure data set using five Voigt peaks. (a) The low-count-rate region enlarged to highlight the Compton shelf region, the minor Compton peak and the weakest fitted central peak. (b) Four dominant peaks are clear in the total intensity profile, (c) leading to a small residual. For this fit,  $\chi_r^2 = 0.427$  with a  $K\alpha_2/K\alpha_1$  peak ratio = 0.511(3).

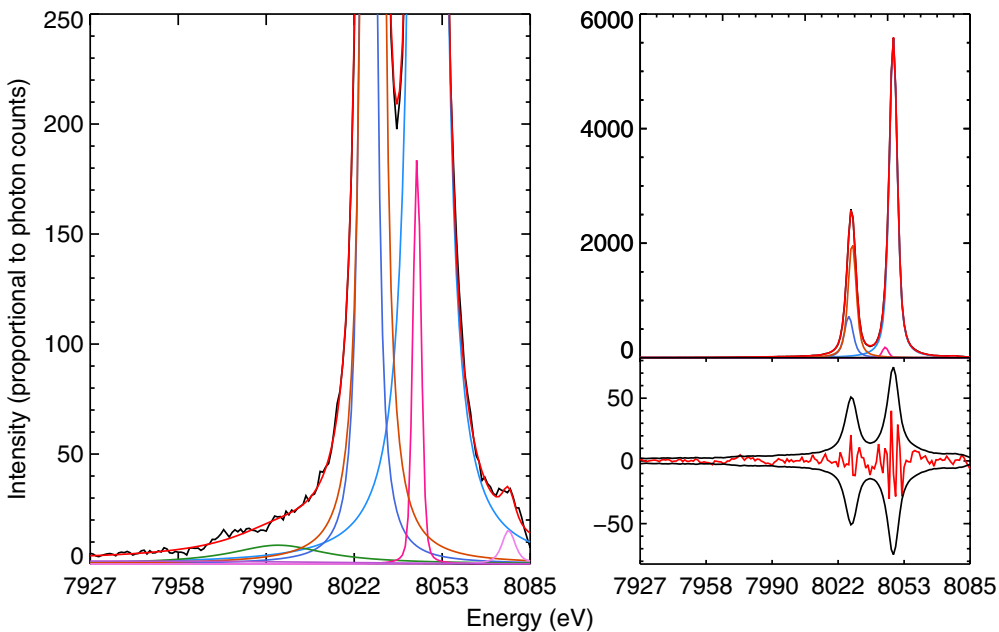


**Figure 4.** A six Voigt peak fit, as compared to a five Voigt peak fit in figure 3 for the same data set. Here,  $\chi_r^2 = 0.252$  and the  $K\alpha_2/K\alpha_1$  peak ratio = 0.514(3). The reduction in  $\chi_r^2$  indicates the significance of the 2p hole spectator peak on the right. This is a new, empirical fit of the 2p satellite (section 6).

least-squares fit was then performed using the new estimates with the previous fitted Voigt set, and the new residual then analysed in the same way, until up to six Voigts were fitted to each profile. The best fit was recorded for each image and for each method (figures 3 and 4).

The  $\chi_r^2$  provided a compelling case for a total number of five or six Voigt profiles in the fit. The sixth Voigt profile includes the small but real 2p-satellite, found and fitted in all 104 sets of data. This procedure yielded a monotonic decrease in the  $\chi_r^2$  with each additional Voigt (table 1).

#### 4. Comparison with literature standards

Hölzer *et al* have provided outstanding reported profiles of major utility to researchers worldwide. They modelled Cu  $K\alpha$  [9] using a profile represented as a sum of Lorentzians with a common slit instrumental broadening. This computationally modelled instrumental profile is complex but they considered it to be equivalent to a slit. They deconvolve this slit function from their experimental profile to obtain their reportable spectrum. The Lorentzian fit of each successive peak was then

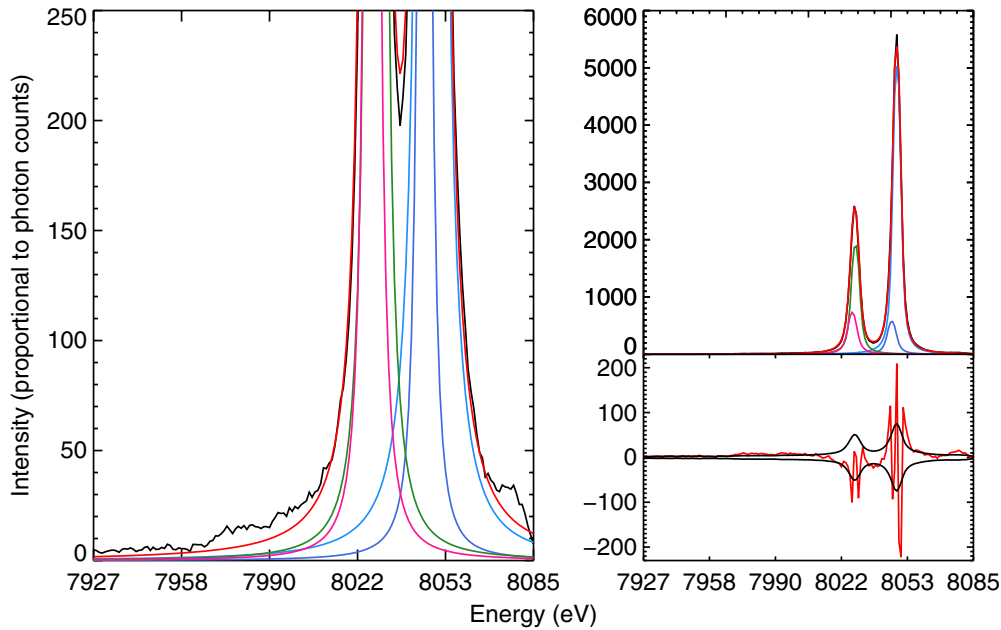


**Figure 5.** Re-creation of the 44 kV, 1000 ms exposure Cu  $K\alpha_{1,2}$  profile using [9]. The profile was reconstructed by convolving the given Lorentzian parameters with a slit function following their experimental methodology. A Levenberg–Marquardt fit was performed to reproduce their profile for our observed spectrum. We confirm that their prescription must be reproduced using a Lorentzian-slit profile, rather than convolution with e.g. a Gaussian, or the profile fails to match observed spectra.

**Table 1.** Monotonic decrease of the  $\chi_r^2$  as the number of peaks increases, for the profile taken at 44 kV with a 1000 ms exposure. The  $\chi_r^2$  reduces monotonically to the noise limit, indicating that, even for the last peak, a real and physical structure has been assigned, and therefore that input counting uncertainties are underestimated.

No. of peaks	$\chi_r^2$
3	0.640
4	0.510
5	0.427
6	0.252

found by locally constraining previous parameters. They were unable to perform a free fit of all parameters.

While the resulting fit is useful and insightful, it is not so readily transferred to other studies and geometries. We need better understanding, especially for the most carefully studied x-ray peak in the literature. To that end, we report (i) the whole Cu  $K\alpha_{1,2}$  profile as collected, and (ii) a free, converged fit of a minimal sum of five Voigts to the Cu  $K\alpha$  profile, together with two components to represent the Compton profile from inelastic scattering in the solid state detector.

Because of the care and significance of the earlier literature, a careful comparison was made with Hölzer *et al* [9]. They also used a single-crystal spectrometer with a Si (111) surface orientation to measure the emission profiles. However they used a collimator of variable but narrow horizontal slit width, the assumption being that the measured profile is a convolution of the true emission profile with the instrumental function [60]. The approximations result in a narrow (slit) mechanical function, which when deconvolved from the emission profile, yields the spectral profile, which was then fit with a sum of Lorentzians.

The Lorentzian sum was constructed by a similar iterative process. However, instead of using our completely relaxed set of parameters, Hölzer *et al* fit each additional Lorentzian to an artificial profile, constructed by removing the profiles of the  $(n - 1)$  Lorentzians from the deconvolved profile. Finally, Hölzer *et al* determined that for Cu there were two  $K\alpha_1$  and two  $K\alpha_2$  components, the smallest number of all the medium  $Z$  elements in their study across the transition metals. No mention of a Compton profile, incomplete charge collection, scattering, nor other broadening effects was made [60].

For comparison of the methodologies, the profile of Hölzer *et al* was recreated using the parameter values provided in their work [9]. The given absolute energy positions and widths were scaled to our profile, and the relative amplitudes and positions given were used relative to the amplitude and position of the corresponding features in our measured profile. The Lorentzians were convolved with a slit function in our Levenberg–Marquardt least-squares methodology to recreate their profile with the functional broadening present in each of our spectra (figure 5). Another recreation of their profile was also produced, using their parameters as before, but including the Compton profile complementary error function (figure 6).

Our six Voigt methodology clearly provides the superior fit as seen in the  $\chi_r^2$  (tables 3 and 4). Both the five and six Voigt models provide better fits than the recreation of Hölzer *et al*, even when the same prescription for the Compton shelf was applied (table 2). Regardless of whether or not the Compton shelf and the 2p satellite peak are addressed, the recreated profiles in figures 5 and 6 show strong residuals in the central peak  $1\sigma$  envelope of much greater significance than in the Compton shelf or high-energy extra peak. Ergo, the Voigt fit methodology describes the characteristic profile better than the Lorentzian-slit methodology employed by Hölzer *et al* in terms of a better representation of the profile,  $\chi_r^2$  and

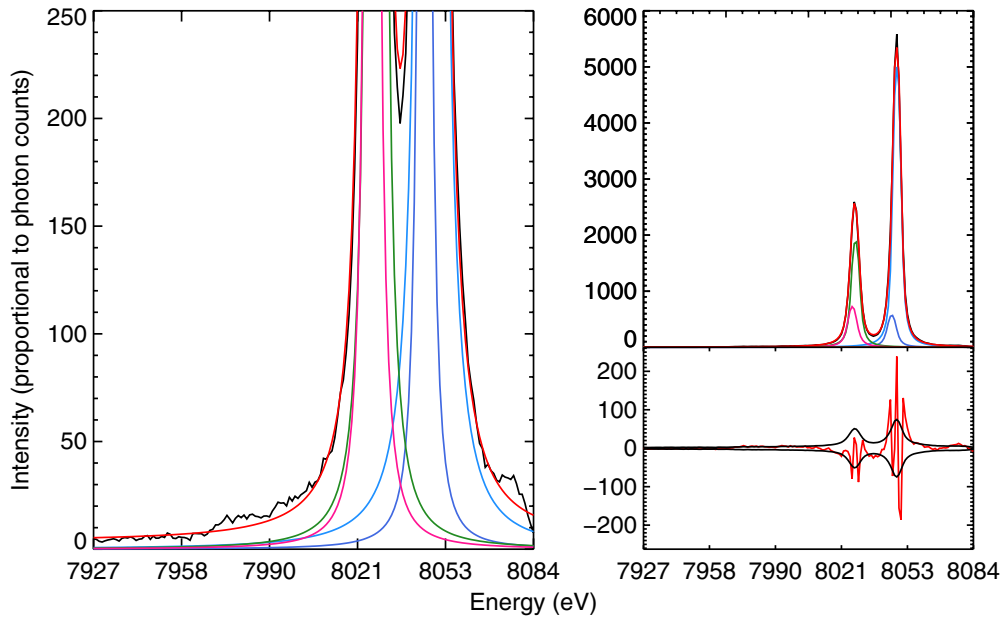


**Figure 6.** Recreation of the Cu  $K\alpha_{1,2}$  profile of Hölzer *et al*, figure 5, with the inclusion of the Compton shelf function. The difference can be seen in the residuals where the inclusion of the Compton shelf function reduces the low-energy residual within the  $1\sigma$  envelope. The approaches both in this work and that of Hölzer *et al* observe and fit four profiles in the central region of the structure.

**Table 2.** The recreated profile parameters of Hölzer *et al* [9], including the Compton shelf function. The recreated parameters maintain their quoted energies, widths, and relative intensities, while the centre of mass, scale, and slit (instrumental) width are specific to fitting our particular emission profile. They provide no slit width or uncertainty, no uncertainty on the (relative) integrated intensities, and each peak was fit independently after subtracting each previous fit from the profile (which neglects correlation and off-diagonal elements of the covariance matrix).

Hölzer <i>et al</i> [9]				
	Centre of mass (eV)	Scale (channels $eV^{-1}$ )	Slit width (eV)	
	8041.002	0.982	3.872	
Central peaks	$K\alpha_{11}$	$K\alpha_{12}$	$K\alpha_{21}$	$K\alpha_{22}$
Peak energies (eV)	8047.837(2)	8045.367(22)	8027.993(5)	8026.504(14)
Peak widths (eV)	2.285(3)	3.358(27)	2.666(7)	3.571(23)
Integrated intensities	0.579	0.080	0.236	0.105
$\chi_r^2$	2.172			
$K\alpha_2/K\alpha_1$ peak ratio	0.517			

**Table 3.** Parameters for the best fit of the shelf function with five Voigts, fitted to the 44 kV, 1000 ms exposure data set: one peak in the shelf region and four in the central peak region as per [9]. The Voigt prescription yields a far improved fit of the spectrum over the similar fit following Hölzer *et al* ( $\chi_r^2 = 0.43$  versus 2.17).

Five Voigt peaks				
	Centre of mass (eV)	Scale (channels $eV^{-1}$ )	Gaussian width (eV)	
	8041.381(640)	0.981(9)	1.212(45)	
Central peaks	$K\alpha_{11}$	$K\alpha_{12}$	$K\alpha_{21}$	$K\alpha_{22}$
Peak energies (eV)	8047.946(58)	8044.217(446)	8028.366(233)	8026.817(362)
Peak widths (eV)	2.517(65)	0.648(166)	2.422(194)	3.080(260)
Integrated intensities	0.649(3)	0.0140(1)	0.216(1)	0.121(1)
$\chi_r^2$	0.427			
$K\alpha_2/K\alpha_1$ peak ratio	0.511(3)			

residual structure, and a more transferable set of peak values. A remaining uncertainty can only be addressed by arbitrary alternate instrumental geometries and broadening. However, the comparison of hypotheses in the current data sets is clear and consistent.

### 5. Robustness of characteristic profile

The relative parameters from the seven best profiles were used to reparameterize all 104 measured spectra. These reparameterizations were then compared to determine the

**Table 4.** Parameters for the best fit of the shelf function with six Voigts, fitted to the 44 kV, 1000 ms exposure data set: one peak in the shelf region and four in the central peak region. The  $\chi_r^2$  improves significantly compared with the five Voigt fit (table 3). This parameterization represents the best fit of the profiles and all data sets. Resultant peak parameters are presented here. The comparative values are the same as in table 3. The Compton peak parameterization is 7992.815(1.65) eV centroid, 43.775(3.73) eV width, and 0.0110(0.000 02) integrated intensity. The 2p satellite peak is given in table 6.

	Six Voigt peaks			
	Centre of mass (eV)	Scale (channels eV <sup>-1</sup> )	Gaussian width (eV)	
	8041.398(422)	0.982(7)	1.230(37)	
Central peaks	$K\alpha_{11}$	$K\alpha_{12}$	$K\alpha_{21}$	$K\alpha_{22}$
Peak energies (eV)	8047.947(54)	8044.142(481)	8028.272(170)	8026.644(311)
Peak widths (eV)	2.484(60)	0.755(101)	2.489(145)	3.089(298)
Integrated intensities	0.646(3)	0.014(1)	0.217(1)	0.112(1)
$\chi_r^2$	0.252			
$K\alpha_2/K\alpha_1$ peak ratio	0.514(003)			

**Table 5.** Comparison of the reparameterizations of different emission profiles using six Voigts (table 4) across the full range for accelerating voltage: 20 kV, 44 kV and 49 kV. The  $\chi_r^2$  consistency and the stability demonstrate the robustness of the data and methodology (figure 7). This parameterization is robust across exciting voltages from 20 kV through 50 kV, without modification, demonstrated here by examples across the range. This leads to significant insight into the physical processes as discussed.

	Reparameterization of a 44 kV, 1000 ms exposure image			
	Centre of mass (eV)	Scale (channels eV <sup>-1</sup> )	Gaussian width (eV)	
	8041.398(25)	0.982(1)	1.230(1)	
Central peaks	$K\alpha_{11}$	$K\alpha_{12}$	$K\alpha_{21}$	$K\alpha_{22}$
Peak energies (eV)	8047.947(18)	8044.142(12)	8028.272(17)	8026.645(18)
Peak widths (eV)	2.484(2)	0.7550(4)	2.489(2)	3.089(2)
Integrated intensities	0.647(1)	0.0140(2)	0.245(2)	0.095(1)
$\chi_r^2$	0.219			
$K\alpha_2/K\alpha_1$ peak ratio	0.514(3)			
	Reparameterization of 49 kV, 1000 ms exposure image			
	Centre of mass (eV)	Scale (channels eV <sup>-1</sup> )	Gaussian width (eV)	
	8041.398(24)	0.982(1)	1.230(1)	
Central peaks	$K\alpha_{11}$	$K\alpha_{12}$	$K\alpha_{21}$	$K\alpha_{22}$
Peak energies (eV)	8047.947(17)	8044.142(12)	8028.272(17)	8026.645(17)
Peak widths (eV)	2.484(1)	0.7550(4)	2.492(1)	3.089(2)
Integrated intensities	0.649(3)	0.014(1)	0.245(2)	0.096(1)
$\chi_r^2$	0.307			
$K\alpha_2/K\alpha_1$ peak ratio	0.514(3)			
	Reparameterization of 20 kV, 2000 ms exposure image			
	Centre of mass (eV)	Scale (channels eV <sup>-1</sup> )	Gaussian width (eV)	
	8041.398(36)	0.982(1)	1.230(1)	
Central peaks	$K\alpha_{11}$	$K\alpha_{12}$	$K\alpha_{21}$	$K\alpha_{22}$
Peak energies (eV)	8047.947(25)	8044.142(18)	8028.272(25)	8026.645(26)
Peak widths (eV)	2.484(2)	0.755(1)	2.489(2)	3.089(3)
Integrated intensities	0.645(4)	0.016(1)	0.247(3)	0.093(3)
$\chi_r^2$	0.453			
$K\alpha_2/K\alpha_1$ peak ratio	0.514(2)			

best method, and the optimal number of additional Voigt profiles. The seven sets of reparameterizations were consistent with one another, within one standard deviation, providing similar parameter values and identical conclusions as to the optimal number of Voigts. Examples are presented in

table 5: four Voigts in the peak region, a 2p satellite and the Compton shelf functional. The best results were obtained by reparameterizing using the 44 kV, 1000 ms exposure data fit. The reparameterizations showed tightly consistent fits throughout all spectra, demonstrating the robustness of the

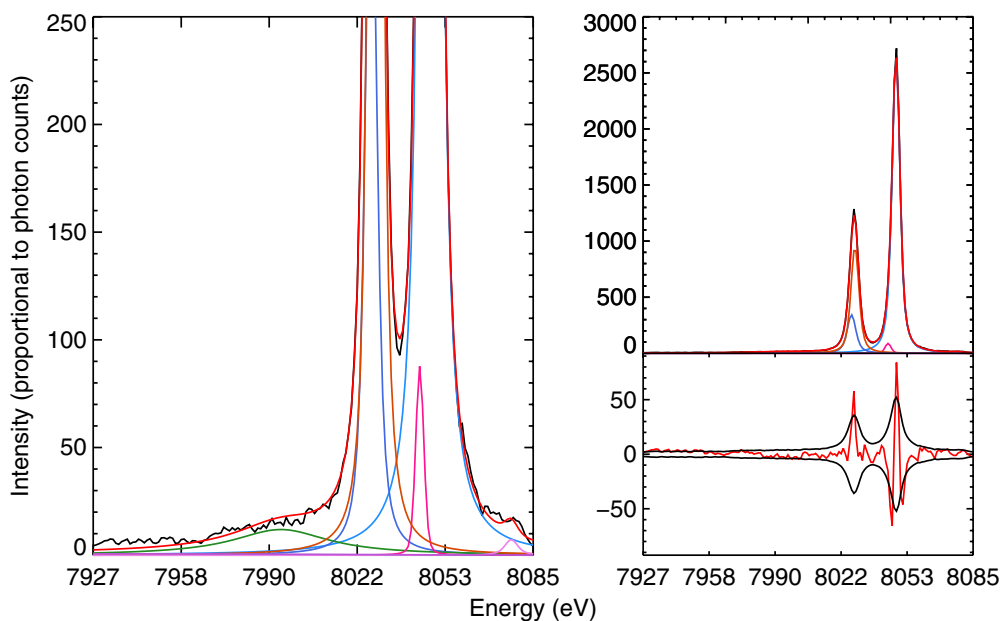


**Figure 7.** Reparameterization of an emission spectrum taken at 20 kV with a 2000 ms exposure. This profile was reparameterized using the optimum six Voigt fit (table 5). The reparameterization gave a consistent result for all exposures and accelerating voltages as illustrated by the residual.

data and method. Our prescription is not dependent upon the selection of any particular fit—it was universal.

It is a significant result that this profile methodology works at all across such a range of accelerating voltages. The accelerating voltage is known to affect the profile, spectrum and peak energies, and changes the profile and peak locations by adjusting the nature and strength of the satellite contributions in the spectrum, which in turn shifts the peaks. Hence naïvely, each fit should be unique, the profile would change continuously with accelerating voltage, and the best fit for one voltage would be inconsistent with that or the data for another voltage. If any defined characteristic spectrum changes with voltage, then exact accelerating voltage in a calibration must be reported, and repeated, to permit a transferable standard. The main tables of Bearden and Burr [61], or of Indelicato and Deslattes [36], provide no such information or insight. These are the main references used in the modern era, but they neither ask nor address the question of robustness, transferability, or the existence of a calibration standard. Original experimental references may provide their accelerating voltages, but stability remains completely unknown. The best work in this area is that of Diamant *et al* [57], proving that the profile is not stable to accelerating voltage, so that the assumption of stability or transferability is in general false.

Crystallographers have for decades suggested that to acquire a robust, stable spectrum, the accelerating voltage needs to be 2.5–3 times the desired characteristic energy or absorption edge energy. We have investigated and measured to high precision the profile dependence across the broader range of 2.5–6.25 times the characteristic energy, in the range of 20–50 kV. The profile is stable to the noise limit. This is a far stronger statement than a ‘rule of thumb’ or the narrow recommended safety range of some suppliers. We

have rigorously quantified the agreement so that the Cu  $K\alpha$  spectrum can indeed be a strong, robust, transferable standard.

More investigation is certainly needed, especially in the range proven by Diamant *et al* to be unstable [57]. These studies are both practical for thousands of practitioners, and provide an insight into atomic and many-body physics. A strong argument for stability in this region of accelerating voltage arises from the validity of the impulse approximation for the transition probabilities, where the liberated photoelectron is considered to be instantaneously removed and does not alter the atomic structure [62]. If the relaxation involves the promotion of a valence electron to a higher unfilled level, the photoelectron undergoes an energy loss that appears in the spectrum as a satellite, shake event, or a peak on the higher binding side of the main transitional energy [21]. Studies of this important area, both experimentally and theoretically, have been sparse.

Our study is not in conflict with Diamant *et al* [57] as their region of instability lies below that of our investigation. Conversely, we confirm for the first time the nature of the stability in the high-energy excitation region. Further studies must investigate more the areas of their earlier insightful investigations. In our high-energy regime, the sudden or impulse approximation should be a reasonable approximation, and the stability we observe proves that this is the case; however, our study does not interrogate the limitations and contributions of shake processes, for example, in the regime where the impulse approximation is no longer valid.

## 6. Characterization of the 2p satellite

Diamant *et al* [57] give a theoretical value for the 2p spectator transition at approximately 30 eV above the  $K\alpha_1$  diagram line. Our peak sits at 8076 eV, consistent with that value. Diamant

**Table 6.** Reparameterizations giving the 2p spectator profile.

44 kV, 1000 ms exposure length		
Peak energy (eV)	Width (eV)	Intensity
8076.623(25)	3.844(3)	0.00215(1)
49 kV, 1000 ms exposure length		
Peak energy (eV)	Width (eV)	Intensity
8076.650(24)	3.848(2)	0.00215(1)
20 kV, 2000 ms exposure length		
Peak energy (eV)	Width (eV)	Intensity
8076.345(38)	3.807(5)	0.00211(6)

*et al* do not give theoretical values for the 2p parameters, but state that this satellite is a group of seven peaks centred at 8080 eV with a total width of  $\sim 10$  eV. The width of our peak is within error of their value. In table 6, the 2p peak parameters are robust across the range of energies. Hence we confirm their findings with different experimental settings.

## 7. Nonlinear noise considerations

The  $\chi_r^2$  in figures 3 and 4 are significantly below 1. However, the true value of the  $\chi_r^2$  test is a monotonic decrease in its value over fit iterations as real physical features are increasingly included in the fit (table 1). This proves indirectly that the assumed normal noise distribution is not adequate for this experimental data. A non-Gaussian noise is the result of not considering shot noise, the Fano factor in the detector, and other possible factors. Fano [42] assumed that the variance in the number of charge carriers in the detector is  $\sigma_n^2 = F\langle n \rangle$  where  $\langle n \rangle$  is the average number of electron-hole pairs produced by incoming x-ray radiation for a fixed energy loss,  $E$ . The Fano factor,  $F$ , accounts for the interdependence of ionization events, i.e. the electron cascade that occurs with an incoming x-ray, causing a reduction in the variance in comparison with Poisson statistics [41]. The Fano factor is then always less than 1. From equation (1),  $\sigma_E^2 = w^2\sigma_N^2 = FwE$  leading to a relationship [63–66] between the peak fwhm

$$\delta E_{\text{fwhm}} = \sqrt{F}\sqrt{8(\ln 2)wE} = 2.355\sqrt{FwE} \quad (3)$$

and the Fano factor,

$$F = \frac{\sigma_{\text{experimental}}^2}{\sigma_{\text{poisson}}^2}. \quad (4)$$

For a Si detector, only about 10% of the total incoming x-ray energy is converted to electron-hole pairs [65]; the remainder is lost to lattice vibrations, phonons and plasmons. Estimates of the Si quantum yield and the Fano factor vary significantly in the literature [43, 44, 65]. Theoretical values for  $F$  in semiconductors disagree with experimentally derived values from a Gaussian treatment of the energy fwhm. Owens *et al* [65] found a theoretical Fano factor of 0.159 for soft x-rays ( $E < 10$  keV), and an experimental Gaussian approximation of 0.142(10) for Si at 170 K, using a quantum yield in Si of 3.679 eV. They attribute the discrepancy to having subtracted off the other sources of noise in quadrature, leading to artificially high values of  $F$ , when they should have been

removed in Fourier space. They note that the low-energy threshold of the detector will narrow peak distributions by filtering out partial energy losses on the low-energy side of the peaks, which will in turn lead to artificially low values of  $F$ . They corrected their approximation by modelling the changes in  $F$  at various energies, and give a final result of  $F = 0.157(2)$ . We note that [65] gives a result at almost the same temperature as our experiment, so is a good estimate for our purposes.

All existing methods of experimentally determining the Fano factor are variations on subtracting in quadrature the electronic noise from the variance in the obtained profile [44, 67, 68]. The energy resolution of the mercuric iodide detector,  $\delta E$  of the fwhm, is defined [69] as

$$(\delta E)^2 = (\delta E_n)^2 + (\delta E_{\text{col}})^2 + (\delta E_F)^2 \quad (5)$$

where  $\delta E_n$  is the electronic noise in the detector amplification system,  $\delta E_{\text{col}}$  is the noise due to incomplete charge collection, and  $\delta E_F$  is the noise due to the statistical charge generation in the detector (the Fano noise). This definition assumes that the three noise contributions follow Gaussian statistics, which is not valid for Fano noise. Modern CCDs are now of sufficient resolution that Fano noise dominates above 1 keV [65], making isolation of Fano contributions from other noise possible. This of course depends on all sources of noise being accurately modelled and calculated.

The importance of considering detector physics, quantum yield and Fano factor must be further investigated. The Fano factor is a function of both detector temperature and the energy of the incident x-rays. A Gaussian decomposition of the peak fwhm may lead to an incorrect evaluation of the Fano factor, since the Fano noise does not follow Gaussian statistics and both of these are functions of the quantum yield. Since the least-squares iterative fitting approach assumes Gaussian ( $\sqrt{N}$ ) noise, we can estimate the effect of the Fano factor and quantum yield uncertainty on figure 4; allowing for it should ideally result in a  $\chi_r^2$  of order 1.

## 8. Discussion and conclusions

We have demonstrated the robustness of the Voigt profile fit to the Cu  $K\alpha$  spectral profile, investigated the nature of broadening, and presented a new and more accurate parameterization suitable for calibration in other experiments. We present a new method of fitting the x-ray emission profiles that consistently fits similar profiles across a wide range of intensities and exposure lengths, implying that Cu  $K\alpha$  can indeed be a highly accurate and transferable standard for energy. Drawing reportable conclusions from such profiles requires a careful understanding of the various x-ray processes that occur in the x-ray source, experimental geometry, and detector physics. The new parameterization is appropriate for calibrations requiring Cu  $K\alpha_{1,2}$  spectra. The Voigt prescription, despite the computational complexity, gives a better and more consistent fit than the previous standard. This methodology can now be applied to other important characteristic radiation including copper K  $\beta$ , but we note that this relative profiling does not depend upon other calibration spectra for its effectiveness.

## Acknowledgments

We would like to acknowledge the group of X-ray and synchrotron science at the School of Physics for their support and assistance.

## References

- [1] Bohr N 1913 On the constitution of atoms and molecules: part I *Phil. Mag.* **26** 1–25
- [2] Bohr N 1913 Part 2 systems containing only a single nucleus *Systems* **1** 1–26
- [3] Niering M *et al* 2000 Measurement of the hydrogen 1S–2S transition frequency by phase coherent comparison with a microwave cesium fountain clock *Phys. Rev. Lett.* **84** 5496–9
- [4] Penrose R 1989 *The Emperor's New Mind* (Oxford: Oxford University Press)
- [5] Chantler C T 2004 Discrepancies in quantum electrodynamics *Radiat. Phys. Chem.* **71** 611–7
- [6] Chantler C T, Kinnane M N, Su C H and Kimpton J A 2006 Characterization of  $K\alpha$  spectral profiles for vanadium, component redetermination for scandium, titanium, chromium, and manganese, and development of satellite structure for  $Z = 21$  to  $Z = 25$  *Phys. Rev. A* **73** 012508
- [7] Chantler C T *et al* 2012 Testing three-body quantum electrodynamics with trapped  $\text{Ti}^{20+}$  ions: evidence for a  $z$ -dependent divergence between experiment and calculation *Phys. Rev. Lett.* **109** 153001
- [8] Chantler C T, Paterson D, Hudson L T, Serpa F G, Gillaspay J D and Takács E 2000 Absolute measurement of the resonance lines in heliumlike vanadium on an electron-beam ion trap *Phys. Rev. A* **62** 042501
- [9] Hölzer G, Fritsch M, Deutsch M, Härtwig J and Förster E 1997  $K\alpha_{1,2}$  and  $K\beta_{1,3}$  x-ray emission lines of the 3d transition metals *Phys. Rev. A* **56** 4554–68
- [10] Williams J H 1933 Relative intensities and transition probabilities of the  $K$ -series lines of the elements 24 to 52 by the ionization chamber method *Phys. Rev.* **44** 146–54
- [11] McCrary J H, Singman L V, Ziegler L H, Looney L D, Edmonds C M and Harris C E 1971  $K$ -fluorescent-x-ray relative-intensity measurements *Phys. Rev. A* **4** 1745–50
- [12] Salem S I and Wimmer R J 1970  $K\alpha_2/K\alpha_1$  transition probabilities in elements with  $Z \sim 50$  *Phys. Rev. A* **2** 1121–3
- [13] Scofield J H 1974 Exchange corrections of K x-ray emission rates *Phys. Rev. A* **9** 1041–9
- [14] Finster J, Leonhardt G and Meisel A 1971 On the shape and width of the main lines of x-ray K emission of the 3d and 4d elements *J. Phys. Colloq.* **32** C4-218
- [15] Chantler C T, Lowe J A and Grant I P 2010 Multiconfiguration Dirac–Fock calculations in open-shell atoms: convergence methods and satellite spectra of the copper  $K\alpha$  photoemission spectrum *Phys. Rev. A* **82** 052505
- [16] Chantler C T, Hayward A C L and Grant I P 2009 Theoretical determination of characteristic x-ray lines and the copper  $K\alpha$  spectrum *Phys. Rev. Lett.* **103** 123002
- [17] Lee P L and Salem S I 1974 Widths and asymmetries of the  $K\alpha_1$  and  $K\alpha_2$  x-ray lines and the  $L_2$  and  $L_3$  fluorescence yields of the transition elements *Phys. Rev. A* **10** 2027–32
- [18] Parratt L G 1936  $K\alpha$  satellite lines *Phys. Rev.* **50** 1–15
- [19] Deutsch M and Hart M 1982 Wavelength, energy shape, and structure of the Cu  $K\alpha_1$  x-ray emission line *Phys. Rev. B* **26** 5558–67
- [20] Maskil N and Deutsch M 1988 Structure and wavelength of the Cu  $K\alpha_2$  x-ray emission line *Phys. Rev. A* **37** 2947–52
- [21] Lowe J A, Chantler C T and Grant I P 2011 *Ab initio* determination of satellite intensities in transition-metal photoemission spectroscopy using a multiconfiguration framework *Phys. Rev. A* **83** 060501
- [22] Meisel A, Leonhardt G and Szargan R 1989 *X-Ray Spectra and Chemical Binding (Springer Series in Chemical Physics vol 37)* ed R Comer (Berlin: Springer)
- [23] Edamoto J 1950 The fine structure of K-series x-ray emission spectra of the elements Mn(25)–Zn(30) and Ge(32) *Sci. Rep. Res. Inst. Tokoku Univ. A* **2** 561–612
- [24] Sorum H 1987 The  $K\alpha_{1,2}$  x-ray spectra of the 3d transition metals Cr, Fe, Co, Ni and Cu *J. Phys. F: Met. Phys.* **17** 417
- [25] Tsutsumi K and Nakamori H 1973 *X-Ray Spectra and Electronic Structure of Matter* (Munich: Fotodruck Frank OHG)
- [26] Parratt L G 1959 Electronic band structure of solids by x-ray spectroscopy *Rev. Mod. Phys.* **31** 616–45
- [27] Shigeoka N, Oohashi H, Tochio T, Ito Y, Mukoyama T, Vlaicu A M and Fukushima S 2004 Experimental investigation of the origin of the Ti  $K\alpha$  satellites *Phys. Rev. A* **69** 052505
- [28] Doniach S and Sunjic M 1970 Many-electron singularity in x-ray photoemission and x-ray line spectra from metals *J. Phys. C: Solid State Phys.* **3** 285
- [29] Tsutsumi K and Nakamori H 1973 *X ray Spectra and Chemical Binding* (Munich: Fotodruck Frank OHG)
- [30] Sauder W, Huddle J, Wilson J and Lavilla R 1977 Detection of multiplet structure in Cu  $K\alpha_{1,2}$  by means of a monolithic double crystal spectrometer *Phys. Lett. A* **63** 313–5
- [31] Deutsch M, Kao C, Förster E, Hölzer G, Huotari S, Härtwig J, Hämäläinen K and Diamant R 2004 X-ray spectrometry of copper: new results on an old subject *J. Res. Natl Inst. Stand. Technol.* **109** 75–98
- [32] Fittinghoff D N, Bolton P R, Chang B and Kulander K C 1992 Observation of nonsequential double ionization of helium with optical tunneling *Phys. Rev. Lett.* **69** 2642–5
- [33] Bryan W A *et al* 2006 Atomic excitation during recollision-free ultrafast multi-electron tunnel ionization *Nature Phys.* **2** 279–383
- [34] Barna I F, Wang J and Burgdörfer J 2006 Angular distribution in two-photon double ionization of helium by intense attosecond soft-x-ray pulses *Phys. Rev. A* **73** 023402
- [35] Lowe J A, Chantler C T and Grant I P 2010 A new approach to relativistic multi-configuration quantum mechanics in titanium *Phys. Lett. A* **374** 4756–60
- [36] Deslattes R D, Kessler E G, Indelicato P, de Billy L, Lindroth E and Anton J 2003 X-ray transition energies: new approach to a comprehensive evaluation *Rev. Mod. Phys.* **75** 35–99
- [37] Deutsch M, Hölzer G, Härtwig J, Wolf J, Fritsch M and Förster E 1995  $K\alpha$  and  $K\beta$  x-ray emission spectra of copper *Phys. Rev. A* **51** 283–96
- [38] Kawai J, Konishi T, Shimohara A and Gohshi Y 1994 High resolution titanium  $K\alpha$  x-ray fluorescence spectra *Spectrochim. Acta B* **49** 725–38
- [39] Chantler C T, Laming J M, Dietrich D D, Hallett W A, McDonald R and Silver J D 2007 Hydrogenic Lamb shift in iron  $\text{Fe}^{25+}$  and fine-structure Lamb shift *Phys. Rev. A* **76** 042116
- [40] Thompson A *et al* 2001 *X-Ray Data Booklet* (Berkeley, CA: Lawrence Berkeley National Laboratory)
- [41] Samedov V V 2011 Theoretical basis for the experimental determination of the intrinsic resolution of a strip detector *X-Ray Spectrom.* **40** 7–11
- [42] Fano U 1946 On the theory of ionization yield of radiations in different substances *Phys. Rev.* **70** 44
- [43] Perotti F and Fiorini C 1999 Observed energy dependence of Fano factor in silicon at hard x-ray energies *Nucl. Instrum. Methods Phys. Res. A* **423** 356–63
- [44] Lowe B G and Sareen R A 2007 A measurement of the electron-hole pair creation energy and the Fano factor in

- silicon for 5.9 keV x-rays and their temperature dependence in the range 80–270 K *Nucl. Instrum. Methods Phys. Res. A* **576** 367–70
- [45] Alig R C, Bloom S and Struck C W 1980 Scattering by ionization and phonon emission in semiconductors *Phys. Rev. B* **22** 5565–82
- [46] Wenzel K W, Chi-Kang L, Petrasso R D, Lo D H, Bautz M W, Ricker G R and Hsieh E 1993 Response of X-UV photodiodes to 1.5–17.5 keV x rays and MeV alpha particles *Rev. Sci. Instrum.* **64** 1723–33
- [47] Barbee T W Jr *et al* 1991 Multi-spectral solar telescope array: II. Soft x-ray EUV reflectivity of the multilayer mirrors *Opt. Eng., Bellingham* **30** 1067–75
- [48] Pehl R H, Goulding F S, Landis F S and Lenzlinger M 1968 Accurate determination of the ionization energy in semiconductor detectors *Nucl. Instrum. Methods* **59** 45–55
- [49] Fraser G W, Abbey A F, Holland A, McCarthy K, Owens A and Wells A 1994 The x-ray energy response of silicon part A. Theory *Nucl. Instrum. Methods Phys. Res.* **350** 368–78
- [50] Briggs D and Riviere J C 1983 *Practical Surface Analysis by Auger and X-Ray Photoelectron Spectroscopy* (Chichester: Wiley)
- [51] Riviere J C and Myhra S 1998 *Handbook of Surface Interface Analysis: Methods for Problem-Solving* (Boca Raton, FL: CRC Press)
- [52] Chantler C T and Deslattes R D 1995 Systematic corrections in Bragg x-ray diffraction of flat and curved crystals *Rev. Sci. Instrum.* **66** 5123–47
- [53] Chantler C T 1992 X-ray diffraction of bent crystals in Bragg geometry: I. Perfect-crystal modelling *J. Appl. Crystallogr.* **25** 674–93
- [54] Chantler C T 1992 X-ray diffraction of bent crystals in Bragg geometry: II. Perfect-crystal modelling *J. Appl. Crystallogr.* **25** 694–713
- [55] Herrera-Gomez A 2011 A double Lorentzian line shape for asymmetric photoelectron peaks *Centro de Investigacion Y de Estudios Avanzados del IPN Unidad Queretaro Internal Report* [www.rdataa.com/aanalyzer/docs/aana/Double-Lorentzian\\_Line-Shape.pdf](http://www.rdataa.com/aanalyzer/docs/aana/Double-Lorentzian_Line-Shape.pdf)
- [56] Eichler S and Krause-Rehberg R 1999 Comparison of experimental and theoretical doppler broadening line-shape parameters *Appl. Surf. Sci.* **149** 227–33
- [57] Diamant R, Huotari S, Hämäläinen K, Sharon R, Kao C C and Deutsch M 2006 The evolution of inner-shell multielectronic x-Ray spectra from threshold to saturation for low- to high-Z atoms *Proc. 20th Int. Conf. on X-ray and Inner-Shell Processes; Radiat. Phys. Chem.* **75** 1434–46
- [58] Campbell J L and Wang J X 2005 Lorentzian contributions to x-ray lineshapes in Si(Li) spectroscopy *X-Ray Spectrom.* **21** 223–7
- [59] Markwardt C B 2009 Non-linear least-squares fitting in IDL with MPFIT *Astronomical Data Analysis Software and Systems XVIII* ed D A Bohlender, D Durand and P Dowler (ASP Conf. Series vol 411) (San Francisco: Astronomical Society of the Pacific) p 251 <http://adsabs.harvard.edu/abs/2009ASPC..411..251M>
- [60] Härtwig J, Hölzer G, Wolf J and Förster E 1993 Remeasurement of the profile of the characteristic Cu  $K\alpha$  emission line with high precision and accuracy *J. Appl. Crystallogr.* **26** 539–48
- [61] Bearden J A and Burr A F 1967 Reevaluation of x-ray atomic energy levels *Rev. Mod. Phys.* **39** 125–42
- [62] Briand J P 1976 Two-electron, one-photon transition energies *Phys. Rev. Lett.* **37** 59–61
- [63] Zullinger H R and Aitken D W 1970 Fano factor fact and fallacy *IEEE Trans. Nucl. Sci.* **17** 187
- [64] Aitken D W 1968 Recent advances in x-ray detection technology *IEEE Trans. Nucl. Sci.* **15** 10–46
- [65] Owens A, Fraser G W and McCarthy K J 2002 On the experimental determination of the Fano factor in Si at soft x-ray wavelengths *Nucl. Instrum. Methods Phys. Res. A* **491** 437–43
- [66] Fano U 1947 Ionization yield of radiations: II. The fluctuations of the number of ions *Phys. Rev.* **70** 44
- [67] Nobumiti I, J Kikuchi, Tadayoshi D and Masayuki K 1992 Fano factor in xenon *Phys. Rev. A* **46** 1676–9
- [68] Owens A, Bavdaz M, Andersson H, Gagliardi T, Krumrey M, Nenonen S, Peacock A, Taylor I and Tröger L 2002 The x-ray response of CdZnTe *Nucl. Instrum. Methods Phys. Res. A* **484** 242–50
- [69] Ricker G R, Vallerga J V, Dabrowski A J, Iwanczyk J S and Entine G 1982 New measurement of the Fano factor of mercuric iodide *Rev. Sci. Instrum.* **53** 53